

# High-speed multi-stage gas-steam turbine with flow bleeding in a novel thermodynamic cycle for decarbonizing power generation

Paweł Ziółkowski<sup>1,\*</sup>, Łukasz Witanowski<sup>2</sup>, Piotr Klonowicz<sup>2</sup>, Dariusz Mikielwicz<sup>1</sup>

<sup>1</sup>Gdańsk University of Technology; Faculty of Mechanical Engineering and Ship Technology; Narutowicza 11/12; 80-233 Gdańsk; Poland, [pziolkowski@pg.edu.pl](mailto:pziolkowski@pg.edu.pl)

<sup>2</sup>Turbine Department, Institute of Fluid-Flow Machinery, Polish Academy of Sciences, ul. Fiszerza 14, 80-231 Gdańsk, Poland,

## Abstract

In the global pursuit of sustainable energy and reduced carbon footprints, advances in power generation techniques play a crucial role, not only in meeting the ever-increasing energy demands but also in ensuring that environmental standards are maintained and that the health of our planet is prioritized for future generations.

In the ongoing quest for sustainable energy solutions, novel high-speed multi-stage gas-steam turbine models were designed to address the challenge of decarbonized power production. The thermodynamic parameters were adopted on the basis of the negative carbon dioxide gas power plant cycle relying on the following main devices, namely: wet combustion chamber, spray-ejector condenser, sewage sludge gasifier and gas-steam turbine. The peculiarities of the present system make the turbine the link of three important devices and its parameters affect the entire thermodynamic cycle. Therefore, it is reasonable to carry out dedicated novel in literature CFD calculations that also take into account the bleeding of the medium for the gasification process.

Two distinct turbine models were introduced: a two-stage turbine achieving speeds of 95 000 rpm with an efficiency of more than 80%, and a five-stage turbine reaching 40 000 rpm with an efficiency of less than 70%. A design assumption of a bleed pressure of 100 kPa and a mass flow rate of 0.1 kg/s was adopted for both models. Computational simulations were utilized, and the turbine stages were selected with the aim of reducing energy losses. Through this work, a significant step towards a carbon-negative future using high-speed turbine technologies was demonstrated, laying the groundwork for further advancements in the field.

**Keywords:** multi-stage axial turbine, high-speed, carbon capture, negative carbon dioxide emissions power plant (nCO<sub>2</sub>PP)

---

\* Corresponding author. E-mail address: [pawel.ziolkowski1@pg.edu.pl](mailto:pawel.ziolkowski1@pg.edu.pl) (P. Ziółkowski)

**Nomenclature**

$\vec{d}$	-	Deformation rate	[1/s]
$e$	-	Specific energy	[m <sup>2</sup> /s <sup>2</sup> ]
$h$	-	Specific enthalpy	[m <sup>2</sup> /s <sup>2</sup> ]
$\vec{g}$	-	Mass forces	[m/s <sup>2</sup> ]
$\vec{I}$	-	Unit tensor (Gibbs' idemfactor)	-
$M_m$	-	Average molar mass	[kg/mol]
$\vec{n}$	-	Normal vector	[-]
$p$	-	Pressure	[Pa]
$R$	-	Individual substance constant	[J/(kgK)]
$\vec{q}$	-	Heat flux	[W/s <sup>2</sup> ]
$\vec{\tau}$	-	Reynolds' turbulent stress (momentum flux)	[Pa]
$T$	-	Temperature	[K]
$\vec{T}$	-	Torque	[Nm]
$\vec{t}$	-	Total momentum flux	[Pa]
$\vec{v}$	-	Velocity	[m/s]
$X_m$	-	Mole fraction of component $m$	[-]
$Y_m$	-	Mass fraction of component $m$	[-]
$\vec{\tau}$	-	Momentum flux of viscous stress	[Pa]
$\vec{\tau}^c$	-	Total irreversible momentum flux	[Pa]
$\mu$	-	Dynamic viscosity	[Pas]
$\rho$	-	Density	[kg/m <sup>3</sup> ]
$\vec{\omega}$	-	Rotational speed	[rpm]

*Abbreviations:*

C - compressor,

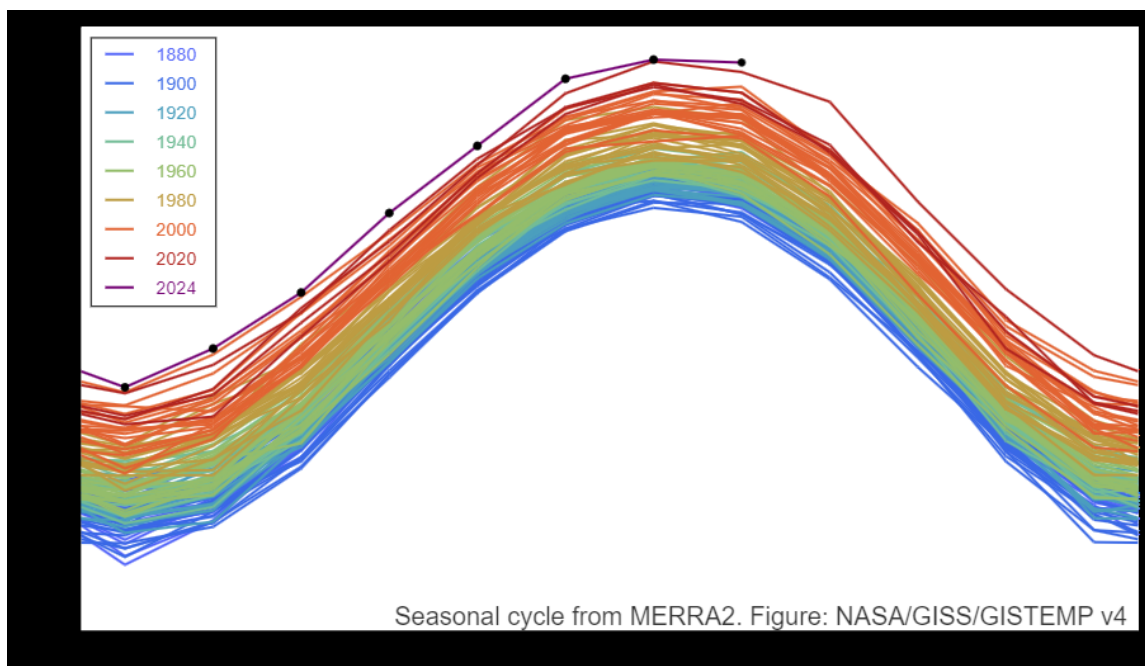
41	CC	- combustion chamber,
42	CCS	- carbon dioxide capture and storage systems,
43	CCU	- Carbon Capture Unit,
44	CES	- Clean Energy Systems,
45	CFD	- Computational Fluid Dynamics, so-called three-dimensional description of unknowns parameters of the power plant devices
46		
47	CHE	- cooling heat exchanger,
48	SEC	- spray-ejector condenser,
49	G	- electric generator,
50	GT	- gas turbine,
51	HE	- heat exchanger,
52	P	- pump,
53	S+CHE	- condensate-cooler heat exchanger and separator,
54	WCC	- wet combustion chamber
55		

56

## 57 1. Introduction

58 According to empirical data from NASA [1,2], July 2023 emerged as a thermodynamic anomaly,  
 59 setting the record for the hottest month ever documented (Fig. 1). The temperature anomaly for that  
 60 month surpassed previous July readings by 0.24°C and stood at 1.18°C above the average July  
 61 temperatures noted during the 1951-1980 baseline period. This data accentuates the urgency of the  
 62 engineering objectives outlined in the Paris Agreement. Grounded in this pact, a firm thermodynamic  
 63 target has been committed to by the global community: the attenuation of anthropogenic factors to  
 64 ensure that the average global temperature does not rise by more than 1.5°C from pre-industrial levels.  
 65 Beyond its geopolitical ramifications, this agreement has galvanized the engineering sector, catalyzing  
 66 a wave of technological breakthroughs.

67



68

69 **Fig. 1** Global temperature anomalies for every July since the 1880s, based on NASA's GISTEMP analysis.  
 70 Anomalies reflect how much the global temperature was above or below the 1951-1980 norm for July [1,2].

71

72 The unprecedented temperature anomaly accentuates the need for efficient renewable energy  
 73 utilization. A key study highlights advancements in energy system modelling for solar and wind power,  
 74 emphasizing the need for higher temporal resolution to address their intermittent nature [3]. For solar  
 75 energy, stochastic and non-dimensional approaches are effective for data downscaling. However, wind  
 76 speed data downscaling is more complex, with current trends favoring a combination of meteorological

77 reanalysis and stochastic methods. Wind energy's role in decarbonizing grids becomes crucial, with  
78 projections suggesting it might account for 40% of energy generation in many regions [4]. However,  
79 this increase leads to challenges like mismatches between generation and grid demand, causing wind  
80 energy devaluation. This is measured by the Value Factor, reflecting a potential 60% loss in revenue  
81 due to intermittency, as seen in US grids with high wind shares. Mitigation strategies include enhancing  
82 grid transmission, government subsidies, and long-duration energy storage. A proposed grid  
83 classification system based on the Net Value Factor (NVF) aims to optimize wind energy systems,  
84 balancing costs with revenue. These approaches are essential for effectively integrating wind power into  
85 increasingly decarbonized grids. Wind energy's role in grid decarbonization is complemented by  
86 photovoltaic (PV) advancements. Accurate PV performance forecasts, essential for grid integration, are  
87 challenged by spectral influences, with errors up to 14% in technologies like polycrystalline silicon [5].

88 Spectral correction functions (SCFs) are employed to address this, with methods based on direct  
89 spectral parameters like average photon energy proving more accurate than proxy-variable methods. A  
90 decision-making framework guides PV modelers, considering climate and system specifics, to improve  
91 forecasting accuracy, crucial for grid efficiency. Alongside wind energy and PV advancements, the  
92 development of Multi Energy Systems (MES) for efficient power management is gaining prominence  
93 [6]. Key to MES optimization is addressing technical constraints and uncertainties, with a focus on  
94 incorporating thermal networks and storage. Recent studies emphasize practical optimization with clear  
95 mathematical formulation and solver choice, balancing descriptive accuracy and ease of  
96 implementation. This approach aids in integrating diverse energy sources into the grid effectively.

97 The global assessment of run-of-river hydropower potentials, considering technical, economic, and  
98 environmental constraints, reveals significant prospects for future energy development. Utilizing  
99 detailed global runoff data and Digital Elevation Models (DEMs), the authors' work [7] estimates a  
100 global exploitable hydropower potential ranging from 5.42 to 39.56 (PWh/yr), depending on flow  
101 dependability. This highlights the importance of precise hydrologic and topographic data in identifying  
102 sustainable and economically viable hydropower sites amidst increasing energy demands.

103 A significant challenge in energy systems is the management of waste heat, showing that 72% of  
104 global primary energy consumption is lost in post-conversion, mainly in electricity generation,  
105 transportation, and industry [8]. Much of this waste heat is available at temperatures below 100 °C,  
106 posing an opportunity for improved energy efficiency. The study proposes a novel approach to estimate  
107 this potential globally, addressing the temperature distribution and exergy content of waste heat. While  
108 there are obstacles like technical constraints and financial barriers, solutions such as the Organic  
109 Rankine Cycle (ORC) [9–11], Organic Flash Cycle [12,13] and heat pumps [14–16] are being explored  
110 for low-grade waste heat recovery. Efficient utilization of waste heat, could significantly enhance energy  
111 systems' sustainability [17].

112 The fight against global warming necessitates a multifaceted approach, incorporating not only  
113 renewable energy sources and systems that effectively utilize waste heat but also pioneering  
114 technologies like the negative carbon dioxide emissions gas power plant (nCO<sub>2</sub>PP) [18]. Advancements  
115 in negative carbon dioxide emissions power plant (nCO<sub>2</sub>PP) technology utilize sewage sludge for  
116 environmentally beneficial electricity generation [19]. A mathematical model is developed to estimate  
117 thermodynamic parameters, focusing on the interaction between gasification and gas-steam turbine  
118 operations. The integration of the gasification reactor with the turbine model significantly enhances  
119 system efficiency. This method shows potential in achieving negative CO<sub>2</sub> emissions and suggests that  
120 increased turbine bleed pressure can further optimize power generation efficiency, contributing to  
121 sustainable and environmentally friendly energy solutions. An important element of this system is the  
122 turbines, or more specifically, their efficiency, which greatly impacts the efficiency of the entire cycle.  
123 These types of turbines are exposed to extreme operating conditions due to the parameters of the working  
124 medium. The temperature of the working medium often exceeds 1000°C, which is extremely important  
125 to consider when designing these types of devices.

126 The authors of the paper [20] examine heat transfer in a high-speed turbine rotor shaft cooling  
127 passage using Computational Fluid Dynamics (CFD) and supercritical CO<sub>2</sub>. Key aspects studied include  
128 coolant temperature, heat transfer coefficient, and the effects of clearance, mass flow rate, shaft  
129 rotational speed, and temperature. Findings reveal that coolant temperature and heat transfer coefficient  
130 are minimally affected by radial clearance, which is significant for turbine design. The study also shows  
131 that convection heat transfer is much higher than frictional heat transfer, indicating a dominant role in

132 cooling efficiency. Utilizing NIST real gas data for CFD simulations, the research finds that convection  
133 heat transfer values predicted by CFD are significantly higher than those predicted by correlation  
134 methods. These insights are crucial for optimizing high-speed turbomachinery, particularly in improving  
135 turbine cooling systems. Developing a high-temperature turbine for supercritical organic Rankine cycle  
136 (SORC) systems, a radial-axial two-stage coaxial design is optimized using Siloxane MM as the working  
137 medium [21]. This turbine achieves an isentropic efficiency of 86.55% at an expansion ratio of 15.37  
138 and is suitable for medium to high temperature ORC systems. The design, validated through 3D  
139 simulations, demonstrates high efficiency and adaptability under various operational conditions,  
140 representing a significant advancement in high-temperature turbine technology for renewable energy  
141 systems. In another analysis [22], finite element methods were used to analyze stress and strain dynamics  
142 in the intermediate-pressure steam turbine rotor. The study aims to identify critical regions and assess  
143 their fatigue life under various operational conditions. Notably, the heat grooves in the balance piston  
144 were found to be prone to cracking. The Prager–Ziegler kinematic hardening model is validated as a  
145 reliable tool for predicting both strain amplitudes and fatigue life, closely aligning with field and non-  
146 destructive test data. A comprehensive review of cooling technologies highlights advancements in both  
147 the scientific and engineering aspects of cooling technology [23]. For numerical simulations, the RANS  
148 approach remains the preferred method, while enhanced measurement tools offer valuable experimental  
149 insights. Significant progress has been achieved in understanding the effects of rotational forces on heat  
150 transfer. Cooling designs have evolved, particularly with promising innovations like lamellar and micro-  
151 scale cooling. Research on disk and cavity cooling specifically targets rotor-stator systems and the  
152 positioning of air injection.

153 With respect to turbine flow systems, there is no work taking into account the nature of the flow in  
154 the area of bleeders, and if CFD analysis is carried out, turbine outlets are the subject to analysis [24–  
155 27]. Typically, in the context of reducing exhaust loss, it is important to include the interaction between  
156 the last stage and the exhaust diffuser. In this work, a simplified bleeding channel was introduced, so  
157 this is an advantage of this work because, in addition to changing the flow rate, the influence of the flow  
158 diffuser is visible. It is also worth mentioning the fact that this work is new also in terms of flow testing  
159 in turbine design, because, as the examples show [28–31], the analyzes are usually conducted in the  
160 context of a channel without changing the flow mass.

161 In other words, CFD analysis performed in this article, cover a literature gap in respect to bleed  
162 for 3D geometry in wide range parameters. The findings from this study are significant not just for their  
163 immediate technical implications but also for their broader impact on sustainable energy production.  
164 The research presents a compelling case for the feasibility and effectiveness of high-temperature  
165 turbines in nCO<sub>2</sub>PP systems, providing a template for future advancements in this field. The meticulous  
166 analysis of stage power, efficiency, and the influence of various operational parameters offers invaluable  
167 guidance for the structural design and optimization of future turbine systems.

168 The primary objective of this study is to design and compare two novel high-speed, high-  
169 temperature turbine configurations while precisely determining the bleed pressure, with a target of  
170 approximately 100 kPa. These turbines exhibit variations in the number of stages and rotational speeds  
171 while sharing a common characteristic in terms of inlet and outlet diameters. The turbines presented in  
172 this work are intended for utilization within an innovative negative carbon dioxide gas power plant  
173 (nCO<sub>2</sub>PP). The results of this study provide a comprehensive understanding of the effects of varying the  
174 bleed level within the range of 0 to 20%, the outlet pressure within the range of 7 to 30 kPa, and the  
175 rotational speed within  $\pm 10,000$  rpm of the design rotational speed. Furthermore, this research  
176 investigates how these parameters impact the overall performance of the turbine.

177



178  
179

## 2. Thermodynamic nCO<sub>2</sub>PP cycle integrated with gasification

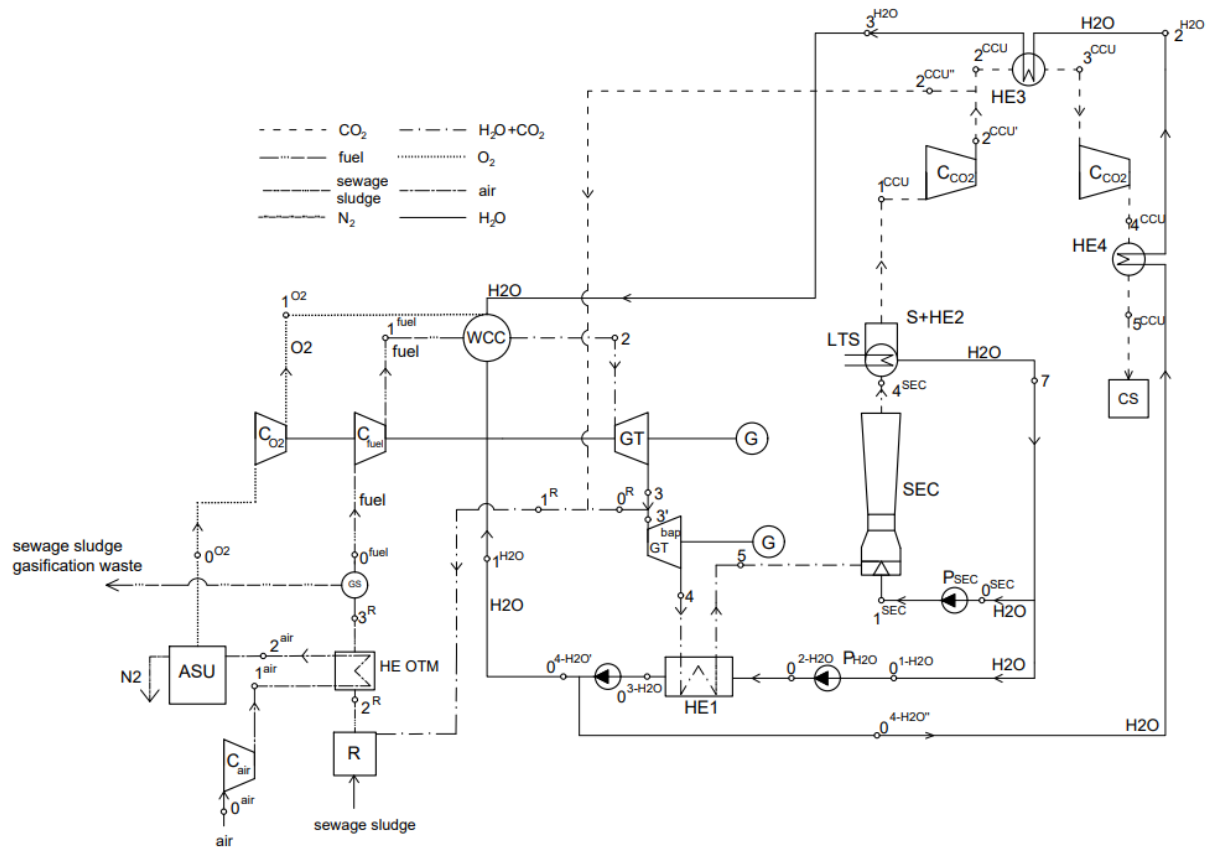
180 Calculations for the nCO<sub>2</sub>PP cycle itself have already been carried out for several power levels with  
181 a distinction between several configurations [19,32–37]. Ziólkowski et al papers [32,33] considered a  
182 156 kWe cycle, but without including the gas turbine bleed, and gasification was from an external heat  
183 source using steam. In [15], the bleed was fully linked to the nCO<sub>2</sub>PP cycle, in such a way that the bleed  
184 stream reached the gasification reactor, where syngas production took place using a converting agent  
185 containing H<sub>2</sub>O and CO<sub>2</sub>. In the aforementioned work [15], the power of the system dropped to 143 kWe  
186 due to a reduction in the power given off by the turbine, but this effect did not take into account the  
187 change in stage efficiency, which is taken into account by CFD calculations. Much higher capacities  
188 were analyzed by Ertesvåg et al. [38] where 2 MWe was considered, which was supposed to correspond  
189 to a power plant adapted to a typical wastewater treatment plant producing 10,000 tons of sludge per  
190 year. The schematic of the devices operating in the nCO<sub>2</sub>PP cycle is shown in Fig.2(a), and in turn the  
191 course of thermodynamic processes in the T-s diagram is illustrated in Figure 2(b).

192 The first points in the cycle can be determined after the fuel and oxygen compressor (C<sub>fuel</sub>, CO<sub>2</sub>).  
193 These direct the fluids to the wet combustion chamber (WCC). In the WCC, combustion takes place  
194 with simultaneous injection of water, resulting in a mixture of CO<sub>2</sub> and H<sub>2</sub>O. In order to maintain the  
195 temperature of the medium at  $T_2=1100^\circ\text{C}$ , the injection of water as a coolant is mandatory. The mass  
196 flux of water (nodal points 0H<sub>2</sub>O, 1H<sub>2</sub>O and 2H<sub>2</sub>O, 3H<sub>2</sub>O) is regenerated contributes to the turbine  
197 efficiency, which is dependent on the mass flux of regenerated heat.

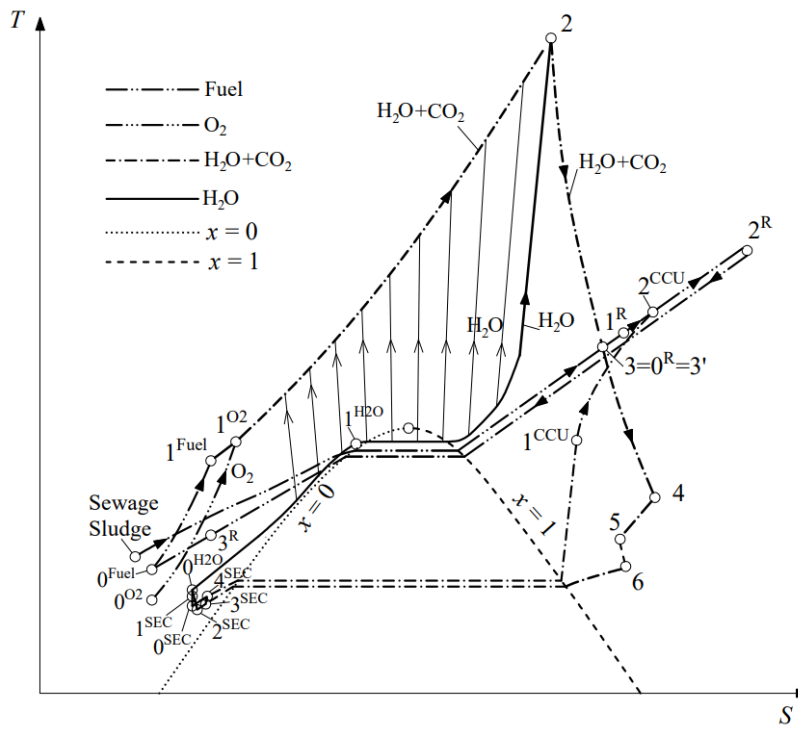
198 After the process in the WCC, the exhaust gas expands in the turbines (GT). The exhaust gas is then  
199 used to heat water, which is transported to the WCC in heat exchanger (HE1). Part of the flue gas stream  
200 is directed to the gasifier (R) and used in the gasification process. An extensive analysis of the impact  
201 of thermodynamic parameters in the extraction point on the syngas production process was carried out  
202 in [15], where the pressure of the extraction point was in the range of  $p_3=0.7 - 1.6$  bar. As a result of the  
203 analysis, it was decided to leave the present parameters at the originally established level, namely at a  
204 bleed pressure of  $p_3=1$  bar and a temperature of  $T_3=672^\circ\text{C}$ .

205 The spray-ejector condenser (SEC) sucks in the exhaust gases from the heat exchanger (HE1). Water  
206 is supplied for the intake and condensation process, which comes from the pump (P<sub>SEC</sub>). The presence  
207 of motive water, which breaks down into droplets to promote direct contact condensation of the mixture  
208 of water vapor and carbon dioxide, namely, enables the process of H<sub>2</sub>O condensation and CO<sub>2</sub>  
209 separation. The uncondensed mixture of water and carbon dioxide SEC goes to the separator with heat  
210 exchanger (S+HE2).

211



212  
213 (a)



(b)

**Fig. 2** The negative emission CO<sub>2</sub> gas power plant (nCO<sub>2</sub>PP): (a) schematic of the devices operating, where: C<sub>O<sub>2</sub></sub> – oxygen compressor, C<sub>fuel</sub> – fuel compressor, WCC – combustion chamber, GT – gas turbine, GT<sup>bap</sup> – low-pressure turbine, HE1 – heat exchanger 1, SEC – spray-ejector condenser, G – generator, P<sub>H<sub>2</sub>O</sub> – water pump, P<sub>SEC</sub> – SEC pump, S+HE2 – separator connected with heat exchanger 2, C<sub>CO<sub>2</sub></sub> – CO<sub>2</sub> compressor, HE3 – heat exchanger 3, HE4 – heat exchanger 4, GS – gas scrubber, R – gasifier, ASU – air separation unit [34], (b) thermodynamic transformations in the T-s diagram [19].

214  
215  
216  
217  
218  
219  
220  
221

222  
223  
224  
225  
226  
227  
228  
229  
230

### 3. Methodology

In this study, two distinct axial turbine designs were developed to meet the specific requirements of a negative carbon dioxide gas power plant integrated with the gasification of sewage sludge [19]. Both solutions (Turbine A and Turbine B) were analysed in an analogous way, namely, first the geometry was created, then mathematical models were used to assess the flow inside the turbine channel, and the final step in the adopted methodology was to change the operating parameters of the turbine.

#### 3.1. Geometries and basic assumptions for Turbine A & Turbine B

The primary challenge in designing these turbines stems from the low mass flow rate of 0.1 kg/s, which necessitates careful consideration of specific speed and manufacturing constraints. The first turbine design, referred to as Turbine A, consists of two stages operating at a high speed of 95,000 rpm. This high speed configuration is essential to maintain adequate specific speed values due to the low volume flow, ensuring efficient energy conversion and minimizing aerodynamic losses. The second turbine design, Turbine B, consists of five stages, each operating at a lower speed of 40,000 rpm. The choice of multiple stages at a reduced speed aims to balance aerodynamic performance with manufacturing feasibility, as lower speeds alleviate some of the technological challenges associated with high-speed machines.

A key design assumption for both turbines is the implementation of a turbine bleed at  $p_3=100$  kPa. This bleed system plays a critical role in controlling flow characteristics and was instrumental in determining the optimal distribution of enthalpy drop across the turbine stages. The bleed pressure influenced stage loading and reaction levels, allowing for tailored aerodynamic performance in each stage. Another important design consideration was the assumption of equal blade heights at the turbine inlet and outlet. This assumption simplifies the mechanical design and manufacturing processes, facilitates consistent flow conditions throughout the turbine, and reduces the complexity of the flow path geometry.

The turbines are designed to operate under the following process conditions: an inlet total pressure of  $p_2=1000$  kPa, an outlet static pressure as low as  $p_4=7$  kPa, and an inlet total temperature of  $T_2=1100$  °C. The extreme pressure ratio across the turbines presents significant aerodynamic challenges, requiring meticulous design to prevent flow separation and ensure stable operation. The calculated reaction degrees were adjusted to be lower by 10% in each stage for the 5-stage turbine and lower by 20% in each stage for the 2-stage turbine, optimizing the balance between the stator and rotor blade loading. Examples of the turbine geometries are shown in Fig. 3 and Fig. 4, while the design parameters of the turbines are summarized in Table 1.

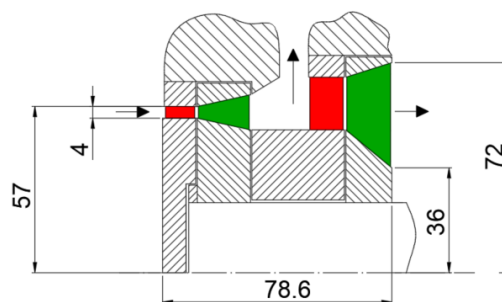
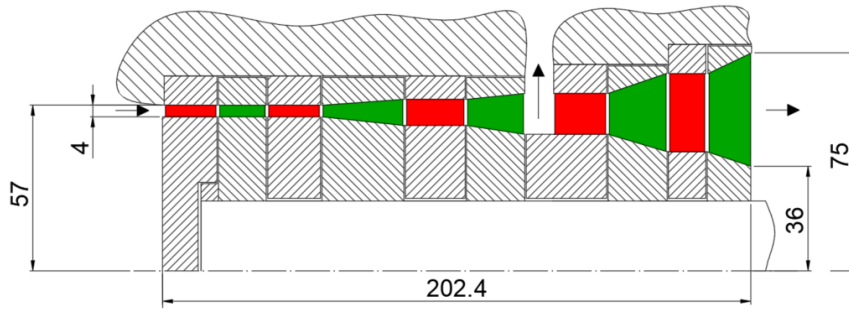


Fig. 3. Meridional section of the baseline two stages axial turbine(stator – red, rotor – green).

The preliminary design was conducted using one-dimensional mean-line analysis, incorporating the Traupel loss model [39,40] to accurately estimate aerodynamic losses. The Traupel model accounts for various loss mechanisms, including profile losses due to blade friction, secondary losses from three-dimensional flow effects, tip leakage losses, and trailing edge and exit losses. By integrating this loss



266 model into the design process, a comprehensive assessment of turbine performance was achieved,  
 267 identifying areas for optimization.  
 268



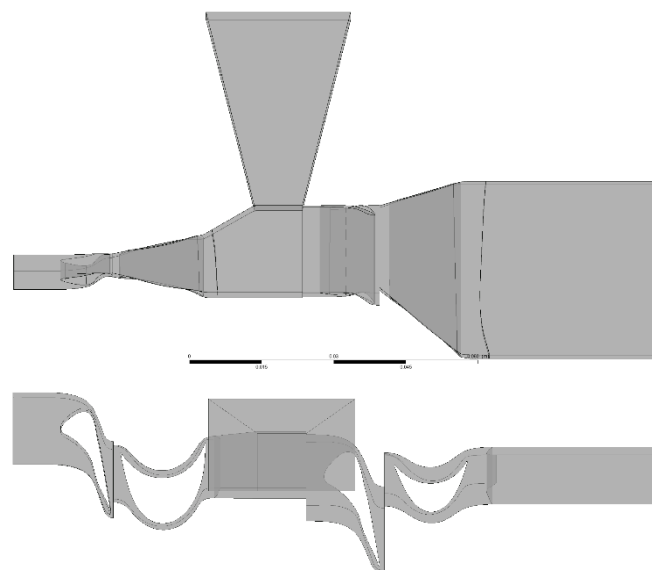
269  
 270 **Fig. 4.** Meridional section of the baseline five stages axial turbine (stator – red, rotor – green).  
 271

272 **Table 1**

273 Design parameters of turbines.

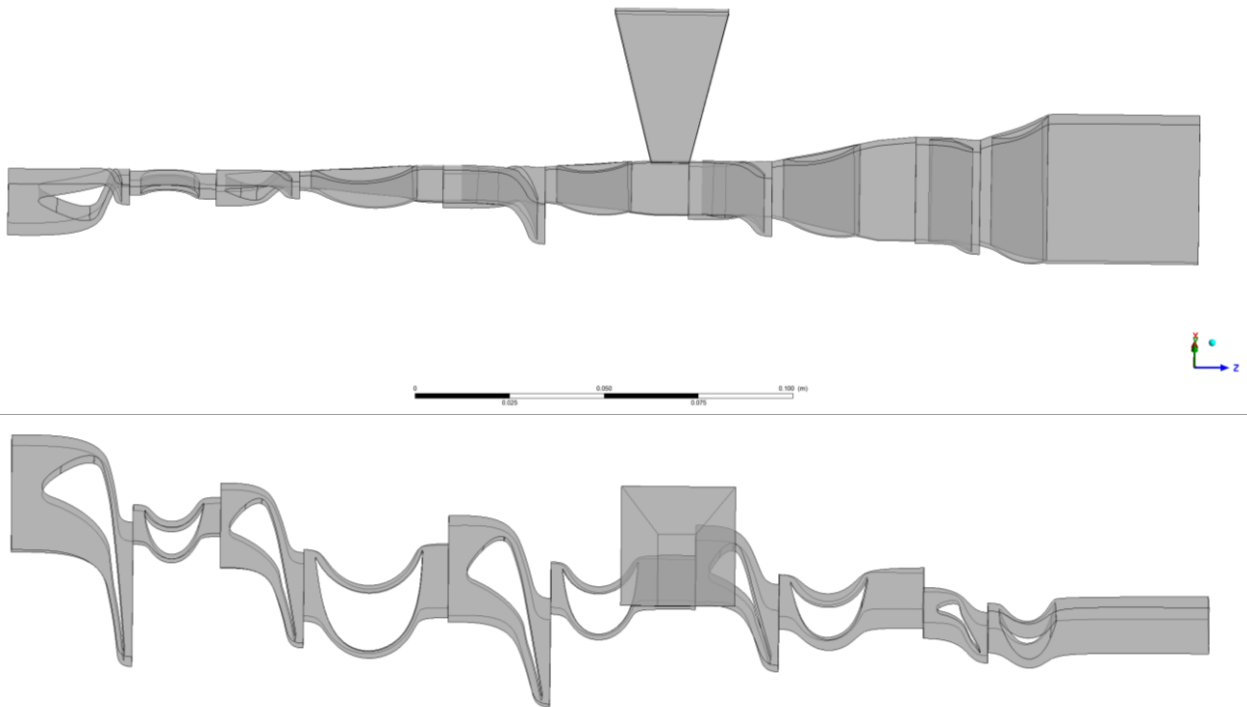
Parameter	Unit	Turbine A	Turbine B
Inlet pressure	[kPa]	1000	
Inlet temperature	[°C]	1100	
Outlet pressure	[kPa]	7	
Mass flow rate	[kg/s]	0.1	
Working fluid	[-]	Mixture of: H <sub>2</sub> -CO <sub>2</sub> -N <sub>2</sub>	
Rotational speed	[rpm]	95 000	40 000
Stages number	[-]	2	5
Bleed pressure	[kPa]	100	

274  
 275  
 276 The flow channels of Turbines A and B are presented in Fig. 5 and Fig. 6. The meridional view of  
 277 the flow expansion (top of Fig. 5) shows a sudden increase in fluid volume especially in the last stage  
 278 of the turbine. In contrast, a view of the blade profiles and the fluid domain on the peripheral slice  
 279 (bottom of Fig. 5) illustrates the inflow and outflow angles in the turbine stages. A meridional view of  
 280 the flow expansion in a five-stage turbine (top of Fig. 6) suggests an orderly growth of the channel cross-  
 281 section. Then, at the bottom of Fig. 6, there is a view of the blade profiles and the fluid domain on the  
 282 peripheral slice. However, in order to fully analyze the behavior of the fluid it is necessary to use the  
 283 mathematical model presented in the next subsection.  
 284



285  
 286 **Fig. 5.** Flow channel of turbine A: two-stage configuration. Meridional view (top) and peripheral slice view  
 287 (bottom).  
 288

289



290

291

292

293

294

**Fig. 6.** Flow channel of turbine B: five-stage configuration. Meridional view (top) and peripheral slice view (bottom).

295

### 3.2. Mathematical model for CFD simulations

296

297

298

299

300

301

302

303

304

305

306

307

308

309

310

311

Subsequent three-dimensional computational fluid dynamics (CFD) analyses were performed to refine the turbine designs and validate the preliminary assessments. The flow domain of each turbine stage was discretized using Ansys Turbogrid software, generating high-quality structured meshes suitable for turbomachinery simulations. Special attention was given to mesh quality parameters to ensure numerical accuracy and convergence. Mesh limits were set on the maximum face angle ( $165^\circ$ ), minimum face angle ( $15^\circ$ ), connectivity number (12), maximum volume ratio (10), minimum volume ratio (0), and maximum edge length ratio (500). These parameters were carefully selected based on mesh sensitivity studies to balance computational cost and solution accuracy. The final computational grid for each turbine comprised several million elements, providing sufficient resolution of the flow features within the blade passages. During the grid independence study, computational meshes with up to 5 million nodes per blade-to-blade passage were investigated. It was found that the maximum relative differences in isentropic efficiency between the finest mesh (5 million nodes) and a mesh with 2 million nodes were less than 0.5% (Fig. 7). This negligible difference indicates that the mesh with 2 million nodes is sufficient to accurately capture the flow characteristics, providing a good ratio between computational efficiency and solution accuracy.

312 The thermal- flow calculations were based on a mathematical model based on a classical system  
 313 of equations, namely mass, momentum and energy balance. The general mass balance equation is  
 314 commonly known by the form [41]:

$$\frac{\partial}{\partial t}(\rho) + \text{div}(\rho\vec{v}) = 0 \quad (1)$$

315 where  $\vec{v}$  is the velocity and  $\rho$  represents density,  $\frac{\partial}{\partial t}$  means derivative in time and  $\text{div}$  depicts  
 316 divergengce. Firstly, taking into account different species the sum of mass fractions of components is  
 317 equal one:

$$\sum_{m=1}^{NS} Y_m = 1 \quad (2)$$

318 Lower index  $m$  indicates the component in the fluid that is assigned the corresponding  
 319 number  $m = 1 \dots NS = \text{H}_2, \text{CO}_2, \text{N}_2$ . Secondly, the same as for molar fractions:

$$\sum_{m=1}^{NS} X_m = 1 \quad (3)$$

320 A further governing equation used in CFD calculations is the momentum balance defined as  
 321 follows [42]:

$$\frac{\partial}{\partial t}(\rho\vec{v}) + \text{div}(\rho\vec{v}\otimes\vec{v}) = \text{div}(\vec{\tau}) + \rho\vec{g} \quad (4)$$

323 Where  $\vec{g}$  is mass force,  $\vec{\tau}$  represents tensor of momentum flux, and  $\otimes$  means dyadic multiplication.  
 324 It should be mention that the total momentum flux is given as:

$$\vec{\tau} = -p\vec{I} + \vec{\tau} + \vec{\tau}^c = -p\vec{I} + \vec{\tau}^c \quad (5)$$

325 Total momentum flux is a sum of pressure with Gibbs idemfactor  $p\vec{I}$ , Reynolds' turbulent flux  $\vec{\tau}^c$ ,  
 326 and tensor of viscous stress defined by Stokes formula [43]:

$$\vec{\tau} = 2\mu \left[ \vec{d} - \frac{1}{3} \text{div}(\vec{v})\vec{I} \right] + \mu' \text{div}(\vec{v})\vec{I}, \quad (6)$$

327 Where  $\mu$  means viscosity,  $\vec{d}$  is a deformation rate describe by equation:

$$\vec{d} = \frac{1}{2}(\text{grad}\vec{v} + \text{grad}^T\vec{v}) = \vec{d}^T, \quad (7)$$

328 The constitutive equations for fluid describing the state of real gas was accomplished according  
 329 information from REFPROP. The total, internal and kinetic energy balance equation in the  
 330 homogeneous mixture model contains the time variations of the quantity to be balanced, the fluxes of  
 331 this quantity leaving (or entering) the control region and the source terms [44]:

$$\frac{\partial}{\partial t}(\rho e) + \text{div}(\rho e \vec{v}) = \text{div}(\vec{q} + \vec{q}^t + \vec{\tau} \vec{v} + \vec{q}^{rad}) + \rho \vec{g} \cdot \vec{v} \quad (8)$$

332 where sum of kinetic and internal energy is  $e = \epsilon + \frac{\vec{v}^2}{2}$ , turbulent, molecular, and radiative heat fluxes,  
 333 respectively  $\vec{q}^t$ ,  $\vec{q}$ ,  $\vec{q}^{rad}$ , mechanical energy flux  $\vec{\tau} \vec{v}$ , and enthalpy of the component per unit mass of  
 334 the component defined as:

$$h_m = \epsilon_m + \frac{p_m}{\rho_m} \quad (9)$$

335 Given that the total momentum flux  $\vec{\tau} = -p\vec{I} + \vec{\tau}^c$  is divided into an elastic reversible part ( $p\vec{I}$ , first  
 336 order derivatives) and a mechanical diffusive part  $\vec{\tau}^c$ , the mechanical momentum flux component  
 337  $-p\vec{I}\vec{v} = -p\vec{v}$  moves to the left-hand side, hence the equation takes the form

$$\frac{\partial}{\partial t}(\rho e) + \text{div}\left[\left(e + \frac{p}{\rho}\right)\rho\vec{v}\right] = \text{div}(\vec{q} + \vec{q}^t + \vec{\tau}^c \vec{v} + \vec{q}^{rad}) + \rho \vec{g} \cdot \vec{v}. \quad (10)$$

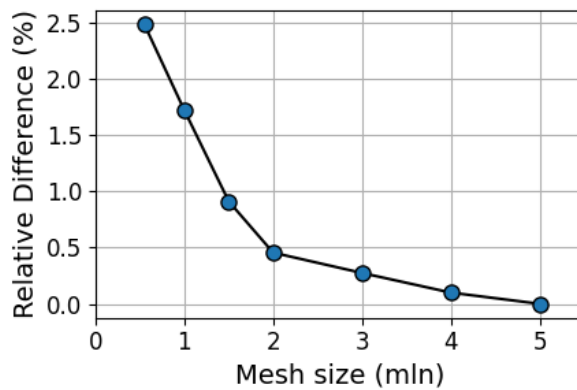
338 The fluid flow in the turbine is adiabatic so we can neglect the components associated with heat  
 339 flux. The enthalpic formulation uses the relationship as follows:

$$\rho e = \rho h + \rho \frac{\vec{v}^2}{2} - p \quad (11)$$

340 where sum of kinetic and internal energy is  $e = \frac{\vec{v}^2}{2} + \epsilon$ . In the literature total enthalpy is described  
 341 by formula:

$$h^c = h + \frac{\vec{v}^2}{2}. \quad (12)$$

342



343

344

345

346

347

348

349

350

351

**Fig. 7** Relative difference between mean values of isentropic efficiency obtained on different grids with respect to the finest investigated grid

Steady-state CFD simulations were carried out using Ansys CFX [45], employing the Reynolds-averaged Navier-Stokes (RANS) equations coupled with the  $k-\omega$  SST turbulence model. The  $k-\omega$  SST model was chosen for its ability to accurately predict flow separation and turbulence effects in turbomachinery applications. A second-order discretization scheme was applied for both the convective and diffusive terms to enhance the accuracy of the numerical solution.

The working fluid properties were modeled using a real gas equation of state, with thermodynamic and transport properties obtained from look-up tables generated using REFPROP version 10 [46]. The real gas model accounts for the non-ideal behavior of the working fluid at high temperatures and pressures, ensuring accurate prediction of density, enthalpy, and other thermodynamic properties critical to turbine performance. Periodic boundary conditions were applied to the sides of the computational domain to simulate the full annulus behavior using a sector model, thereby reducing computational effort. Since the simulations were steady-state, transient rotor-stator interactions were not modeled. Instead, the frozen rotor approach was employed to approximate the interaction between stationary and rotating components. The frozen rotor method maintains the relative positions of the rotor and stator blades fixed, capturing the circumferential variations of flow properties at the interface without time-averaging. Boundary conditions were specified as follows: total pressure, total temperature, and flow direction were imposed at the turbine inlet; static pressure was specified at the outlet; rotational speed was applied to the rotor domains; and mass flow rate was defined at the bleed outlet.

The flow fields obtained from the CFD simulations were analyzed to assess key performance metrics such as total-to-static efficiency, stage loading, reaction degree, and secondary flow effects. Validation of the proposed approach and the associated computational model took place in authors' preceding work, where the results of CFD calculations were compared with the measurements and construction of real machines [47,48].

### 3.3. Parameter variations and presentation approach

Calculations were performed for various bleed mass flow rates ranging from 0% to 20% of the total mass flow to assess the impact of bleed on turbine performance. Additionally, both turbines were evaluated without bleed at their respective design rotational speeds. Specifically for Turbine A, further analyses were conducted at different rotational speeds and outlet pressures for each selected bleed level to investigate the sensitivity of turbine performance to these operating parameters.

The integral parameter that links the 3D CFD approach to the design calculations is the isentropic total-to-static efficiency which can be described as follows [49]:

$$\eta_{ts} = \frac{h_{2T} - h_{4T}}{h_{2T} - h_{4sT}} \quad (13)$$

where  $h_{2T}$  is specific total enthalpy at the inlet to turbine in respect to design approach,  $h_{4T}$  and  $h_{4sT}$  represents specific total and isentropic enthalpy, respectively, at the outlet from turbine (See Fig 2). As presented in Figure 3, in the case of Turbine A two-stage, the bleed after the first stage corresponds to the bleed in Figures 2 and 3. And in the case of Turbine B multi-stage, on the other hand, the bleed is after three stages, so this definition can easily be referred to a group of stages or to a single stage. Additionally, the isentropic total-to-total efficiency is determined as follows:

$$\eta_{tt} = \frac{h_{2T} - h_{4T}}{h_{2T} - h_{4sT} - \frac{c_4^2}{2}} \quad (14)$$

where, in addition, there is the turbine absolute velocity (velocity in a stationary reference frame) expressed as a variable in terms of 0D.

During the analysis of integral parameters, results related to power were analyzed first. Normalized turbine power is defined as:

$$N_n = \frac{N_{var}}{N_{without\ bleed}} = \frac{\vec{\omega} \vec{T}}{\vec{\omega} \vec{T}_{without\ bleed}} \quad (15)$$

where  $\vec{\omega}$  is rotational speed and  $\vec{T}$  means torque.  $N_{var}$  is turbine power in variable conditions, especially during bleed process.  $N_{without\ bleed}$  represents the turbines without bleed. Therefore, the turbine power in most general way described as follows:

395

$$N_{var} = \vec{\omega} \vec{T}. \quad (16)$$

396

397 Then, normalized stage power is as follows:

398

$$N_{n\ stage} = \frac{N_{var\ stage\ no}}{N_{without\ bleed\ stage\ no}}. \quad (17)$$

399

400 where  $N_{without\ bleed\ stage\ no}$  represents stage of the turbines without and  $N_{var\ stage\ no}$  is stage power401 in variable conditions in which  $no = 1, 2$  for Turbine A and  $no = 1, \dots, 5$  for Turbine B. bleed .

402 However, the power ratio has been defined only for two stage turbine (Turbine A) in the following

403 equation:

$$N_{stages\ ratio} = \frac{N_{stage\ 2}}{N_{stage\ 1}}. \quad (18)$$

404

405 Furthermore, normalized total-to-static efficiency in turbines can be find as follows:

406

$$\eta_{ts\ n} = \frac{\eta_{ts\ var}}{\eta_{ts\ without\ bleed}}. \quad (19)$$

407

408 where  $\eta_{ts\ var}$  total-to-static efficiency in turbines for variable conditions and  $\eta_{ts\ without\ bleed}$ 

409 represents total-to-static efficiency in turbines for conditions without bleed.

410 Flow visualization techniques were employed to identify regions of flow separation, high turbulence

411 intensity, and potential loss mechanisms. The results provided valuable insights into the aerodynamic

412 behavior of the turbines under various operating conditions, informing further design refinements.

413 By integrating detailed aerodynamic modeling, rigorous mesh generation criteria, and

414 comprehensive CFD analyses, the methodology established a robust framework for designing axial

415 turbines operating under challenging conditions of low mass flow rates and high pressure ratios. This

416 approach ensures that the final turbine designs achieve optimal performance while meeting the

417 technological constraints of manufacturing and operation in a negative carbon dioxide gas power plant.

418

## 4. Results and discussion

419

### 4.1. Performance analysis under different turbine bleed conditions

420

421 A two-stage turbine operating at a speed of 95,000 rpm achieved 122.9 kW with an efficiency of

422 81.5% (turbine A), while a five-stage turbine achieved 99.5 kW with an efficiency of 62.7% (turbine

423 B). The use of a bleeder significantly changes the turbine parameters, as presented in the section below.

424 The normalized turbine power and normalized total-to-static efficiency are presented in Fig. 8-8. In

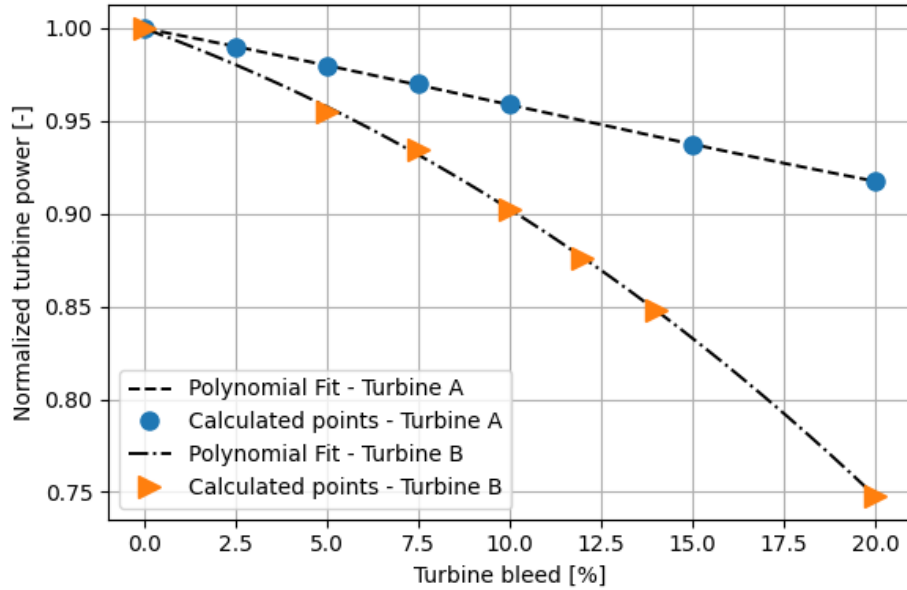
425 the result figures, the dashed line represent results obtained with turbine A, and the dashed dot line

426 represent the results with turbine B. The power drop in turbine B is greater, despite the higher increase

427 in normalized efficiency. However, this increase does not compensate for the significantly lower base

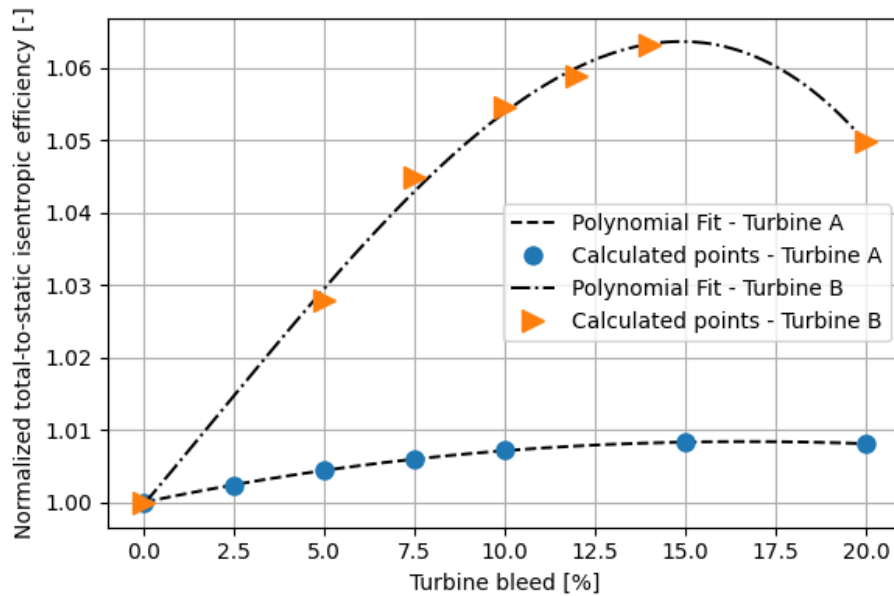
428 efficiency of turbine B, especially considering the potentially lower efficiency of the stages located

429 immediately after the bleeder.



430  
431

Fig. 8. Normalized power in turbines.



432  
433  
434  
435  
436  
437  
438  
439  
440  
441

Fig. 9. Normalized total-to-static efficiency in turbines.

Fig. 10 shows the normalized stage power in turbine A. In the result figure, the dashed line represents results obtained with stage 1 of turbine A, and the dashed-dot line represents the results with stage 2 of turbine A. A slight increase in the power of the first stage is attributed to a change in the operating parameters of the medium and a small local pressure reduction, which enables a greater enthalpy drop to be utilized. Conversely, the significant decrease in power of the second stage primarily results from a lower mass flow of the working medium through this stage.

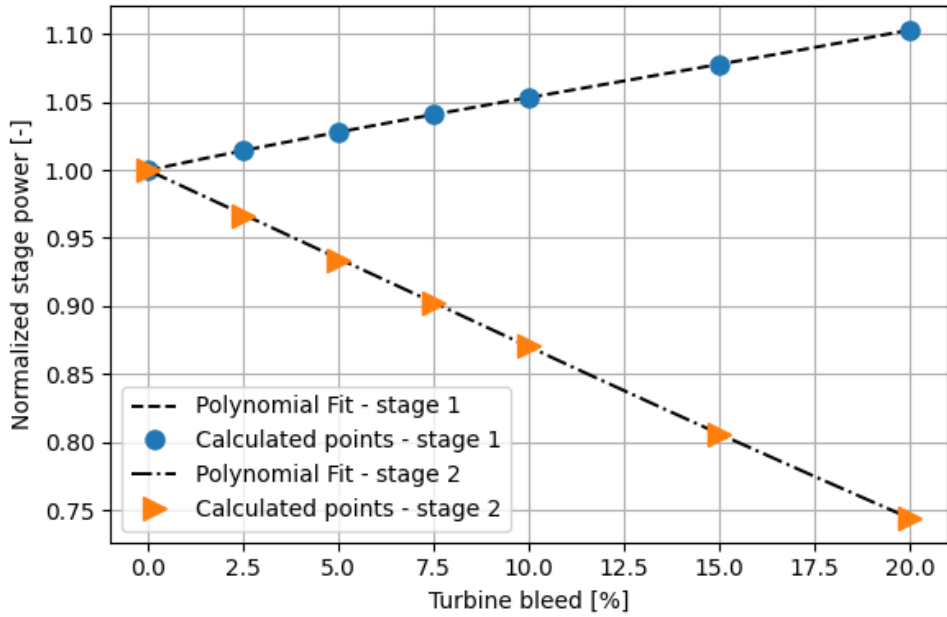


Fig. 10. Normalized stage power in turbine A.

The normalized stage power in turbine B is shown in Fig. 11. A similar trend is evident, as observed in the case of a two-stage turbine (turbine A), where the stages prior to the bleeder exhibit a slight increase in power or maintain a similar level as the bleed level increases. Conversely, the power in stages 4 and 5 decreases by up to nearly 50% and 60%, respectively, with a 20% reduction of the mass flow.

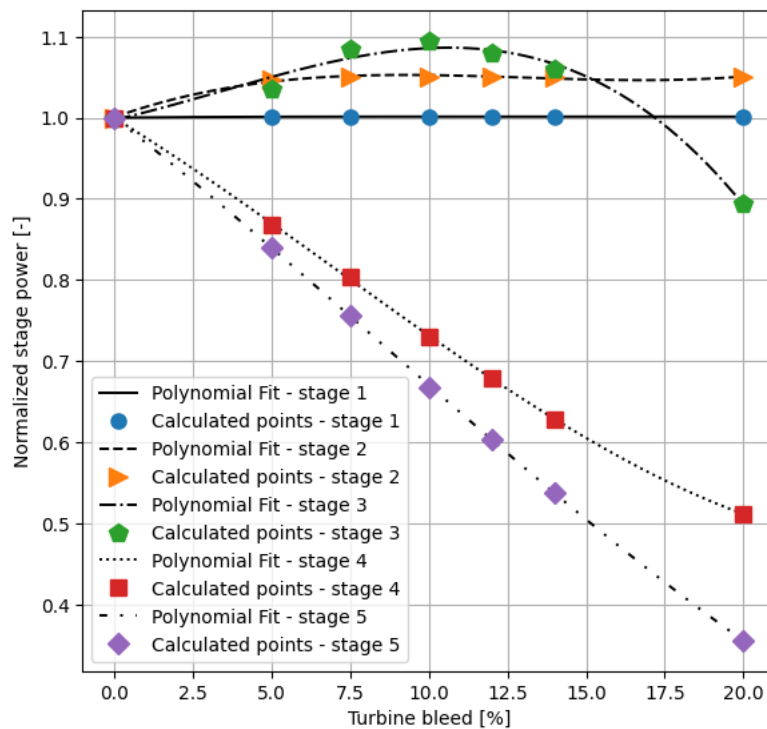


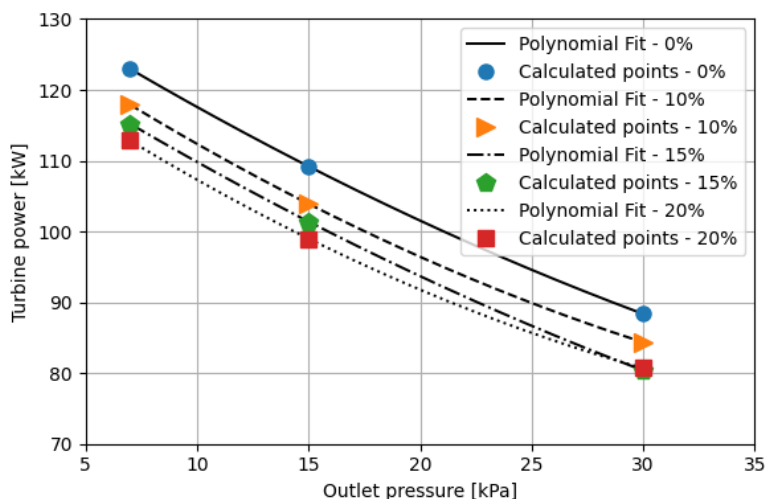
Fig. 11. Normalized stage power in turbine B.

#### 4.2. Performance analysis under different outlet pressure conditions

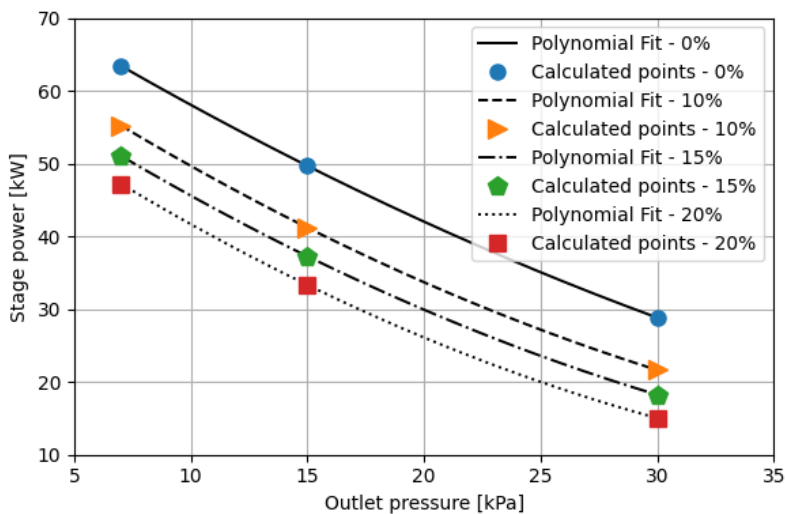
In Fig. 12-Fig. 15, the impact of turbine outlet pressure on various aspects of turbine A is presented. These aspects include the overall power of turbine A, the power across its individual stages, its efficiency, and the power ratio. It is observed that as the outlet pressure increases, turbine A's power



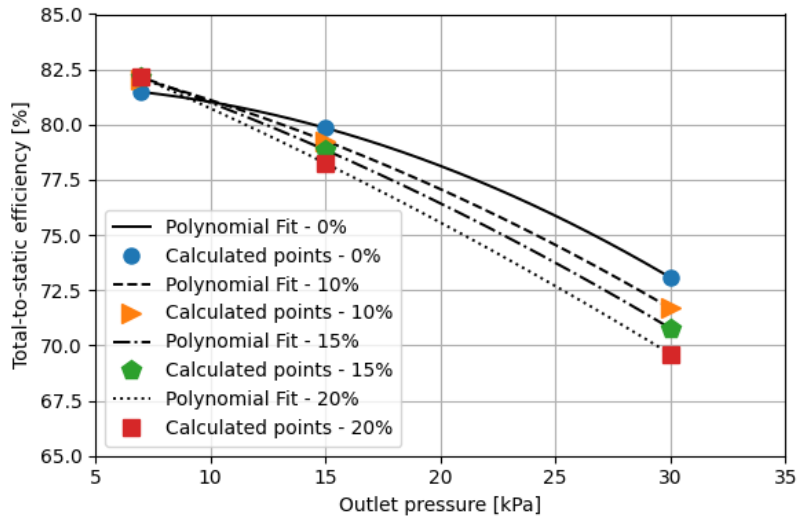
456 decreases almost linearly at all bleed levels. A similar trend is noted in the case of second-stage power.  
 457 At the design point, turbine A's efficiency is the lowest when operating with a bleeder; however, it  
 458 achieves higher efficiency values under broader characteristics (increasing outlet pressure) without a  
 459 bleeder. The power ratio, defined as the ratio of second-stage power to first-stage power, tends to  
 460 decrease. Without bleed at the design point, this power ratio is approximately 1.1, dropping to 0.5 at an  
 461 outlet pressure of 30 kPa. Even lower values are recorded when the turbine operates with a 10%, 15%,  
 462 and 20% reduction. At the highest bleed level and an outlet pressure of 30 kPa, the power ratio  
 463 approaches 0.2. This value is critically important for structural design and the selection of turbine  
 464 bearings.



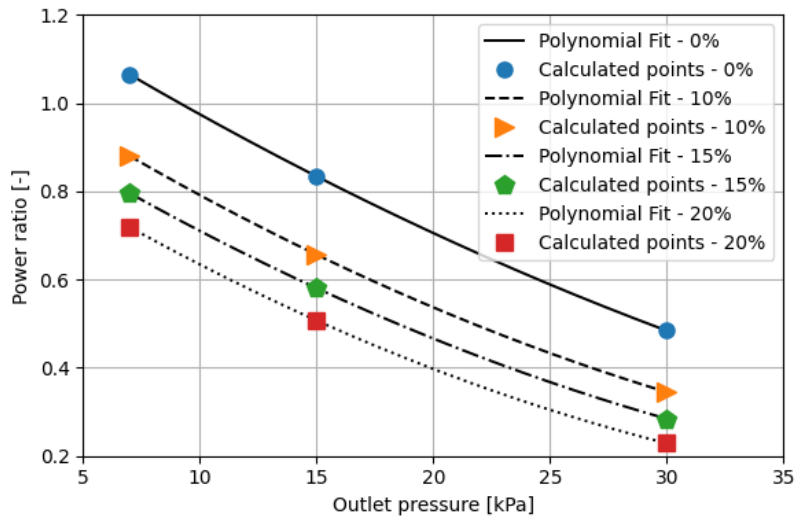
465 **Fig. 12.** Turbine power versus outlet pressure in turbine A for a different bleed level.  
 466



467 **Fig. 13.** Stage power versus outlet pressure in second stage in turbine A for a different bleed level.  
 468  
 469



470  
471 **Fig. 14.** Total-to-static efficiency versus outlet pressure in turbine A for a different bleed level.  
472



473  
474 **Fig. 15.** Power ratio (second stage to first stage) versus outlet pressure in turbine A for a different bleed  
475 level.  
476

477 **4.3. Performance analysis under different rotational speed conditions**

478 The impact of rotational speed on the efficiency, power, and power ratio of the turbine is depicted  
479 in Fig. 16-Fig. 18. An increase in nominal speed leads to higher efficiency in all analyzed cases.  
480 However, unlike the scenario where the influence of outlet pressure was analyzed, the turbine operating  
481 without a bleeder does not achieve significantly higher efficiency values. The increases in power and  
482 changes in power ratio are nearly identical across all cases. Notably, the variation in power ratio is  
483 marginal.

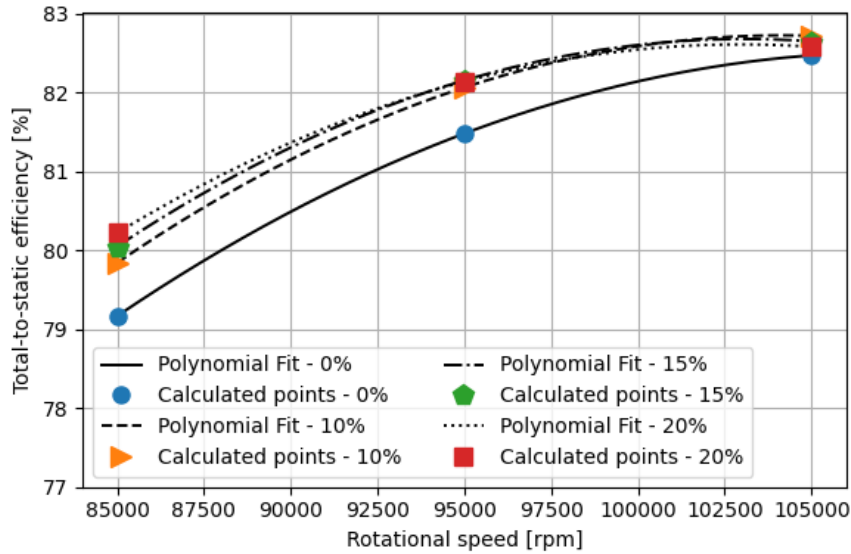


Fig. 16. Total-to-static efficiency versus rotational speed in turbine A for a different bleed level.

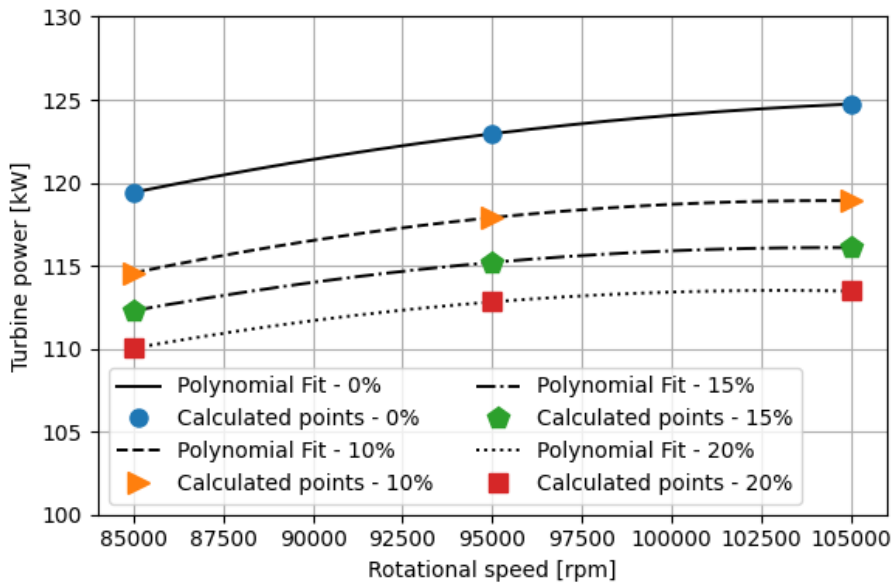


Fig. 17. Turbine power versus rotational speed in turbine A for a different bleed level.

Furthermore, the power and efficiency of turbines A and B were compared (Fig. 19-Fig. 20). At the nominal speed, turbine A achieved significantly higher efficiency (81.5%) and, consequently, higher power (122.9 kW). However, when operating at turbine B's nominal speed of 40 000 rpm, turbine A's efficiency drops to 51.7%, which is lower than turbine B's efficiency of 62.3%. In both turbines, an increase in rotational speed results in an increase in efficiency and power. Finally, the power ratio of turbine A as a function of its rotational speed is also presented (Fig. 21). At a speed of 40 000 rpm, the power ratio reaches 1.22, whereas at 105 000 rpm, it decreases to 1.06

484  
485  
486

487  
488  
489  
490  
491  
492  
493  
494  
495  
496  
497

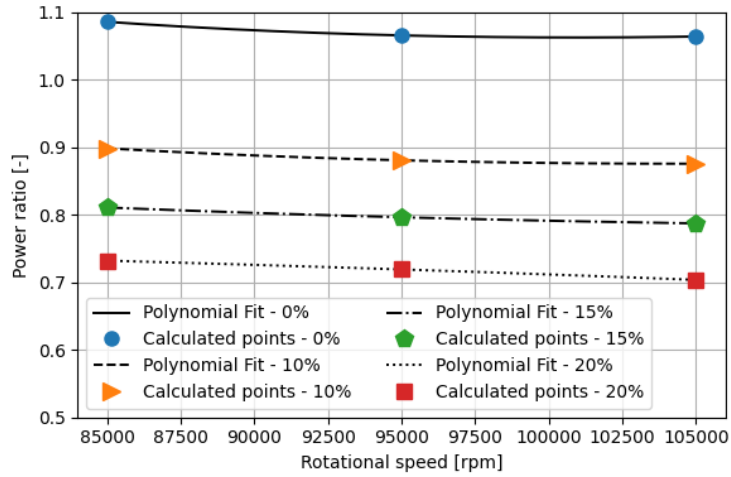


Fig. 18. Power ratio (second stage to first stage) versus rotational speed in turbine A for a different bleed level.

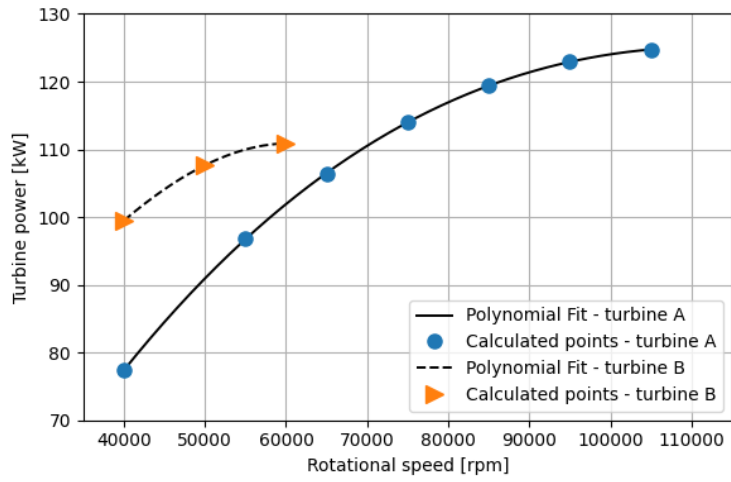


Fig. 19. Turbine power versus rotational speed in turbines.

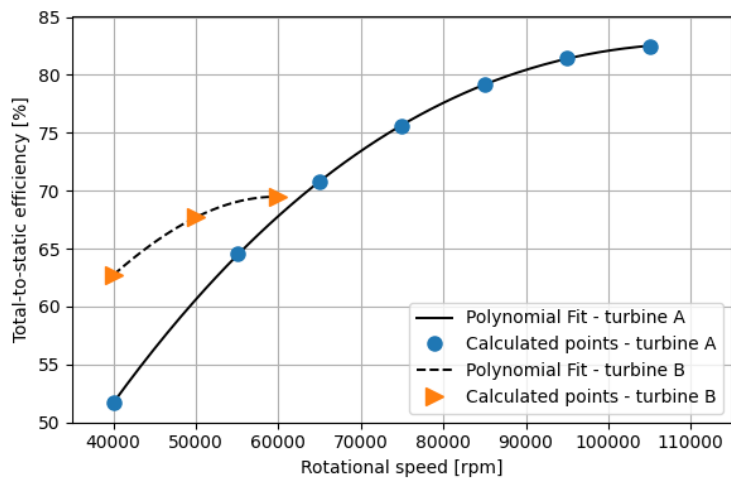


Fig. 20. Total-to-static efficiency versus rotational speed in turbines.

498  
499  
500  
501

502  
503  
504

505  
506

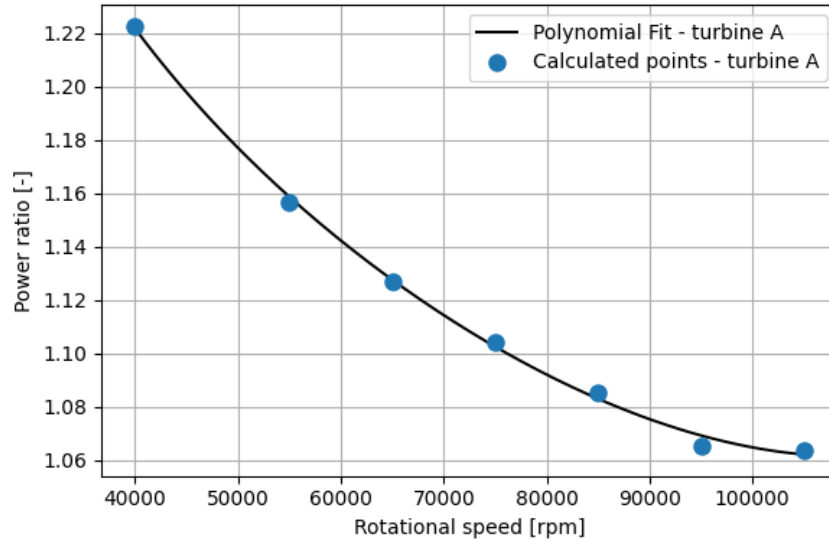


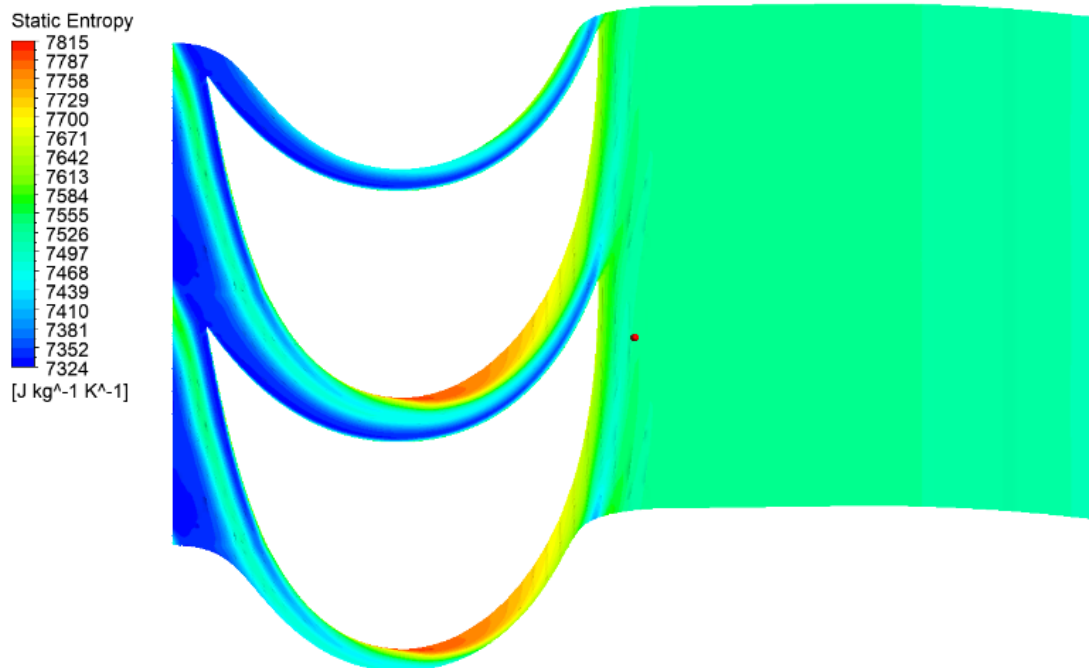
Fig. 21. Power ratio (second stage to first stage) versus rotational speed in turbine A.

It is worth mentioning at this point that similar power outputs as shown in Figure 18 have been analyzed for other biomass systems. In particular, the literature describes the case of 250 kWe, where it was assumed to use such solutions as: 1) gasification and reciprocating engine; 2) gasification and reciprocating engine, with low grade heat extracted from water jacket [50].

#### 4.4. Detailed analysis

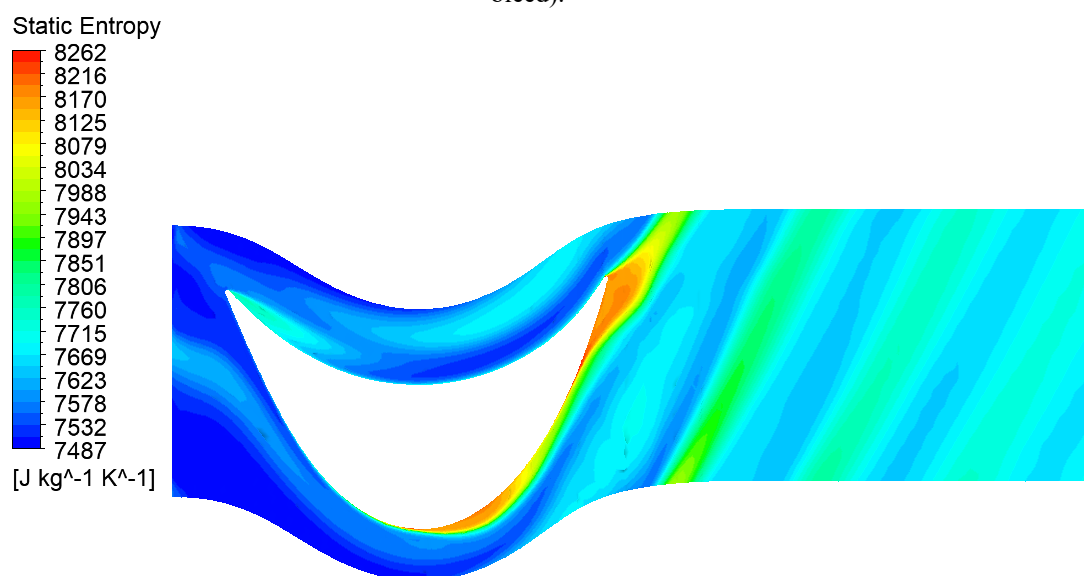
The flow through the channels is characterized by detachment of the stream, at the suction part of the blade, as illustrated in the entropy contours in Fig. 22-Fig. 23. Additionally, a high entropy region at the trailing edge appears in rotor stage 2 (Fig. 23). This region is the main source of losses in the analyzed flow. Therefore, it requires further design and optimization work aimed at reducing profile losses and trailing edge losses across a wide range of flow characteristics. Successful optimization of turbines operating in condensing and cogeneration modes was achieved in previous research [51]. This optimization utilized a Pareto front approach, providing a comprehensive overview of potential solutions and enabling the attainment of measurable benefits.

The velocity vectors for various bleeder operating conditions are illustrated in Fig. 24-Fig. 26. A notable area of fluid mixing is observed, resulting from the oversized dimensions of the bleeder, particularly when operating the second stage of the turbine at significantly lower loads. Future research can include a transient analysis of the medium flow through the turbine, focusing on the changing flow through the bleeder. However, this CFD analysis gives information about the nature of the flow and the direction of further action particularly relevant to new technical solutions whether for nCO<sub>2</sub>PP cycle [19] or other unusual turbines such as two-phase reaction turbine [52] and radial inflow turbine for ocean thermal energy [53].



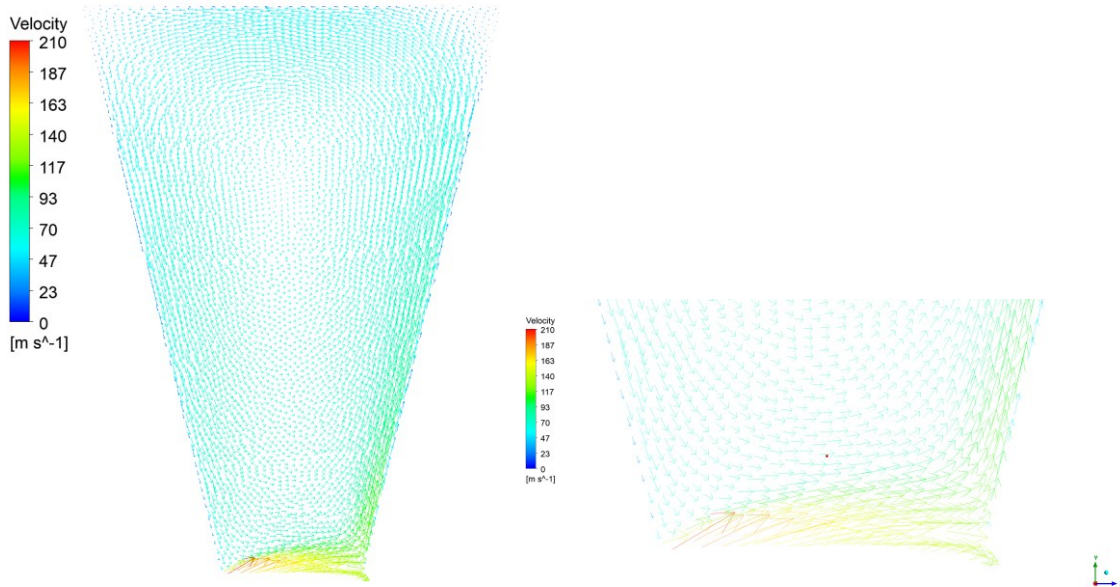
532  
533  
534

**Fig. 22** Static entropy contours in the stage 1 rotor at the mid span (operating in a mode with 20% of mass bleed).

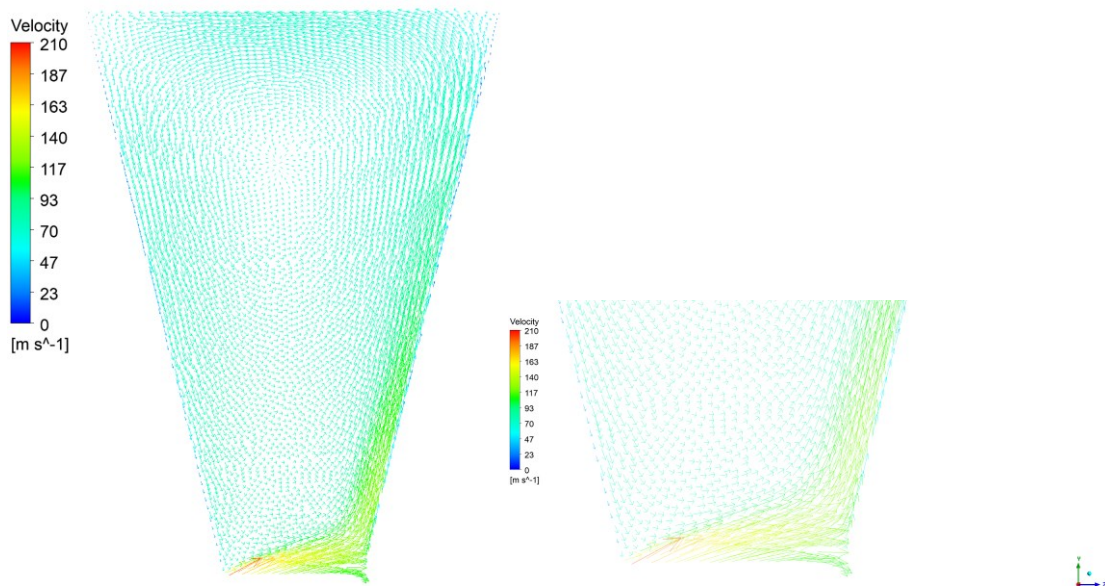


535  
536  
537  
538

**Fig. 23** Static entropy contours in the stage 2 rotor at the mid span (operating in a mode with 20% of mass bleed).



539  
 540 **Fig. 24** Velocity contours in bleed domain without mass flow output.  
 541



542  
 543 **Fig. 25** Velocity contours in bleed domain with 10% of mass flow.  
 544

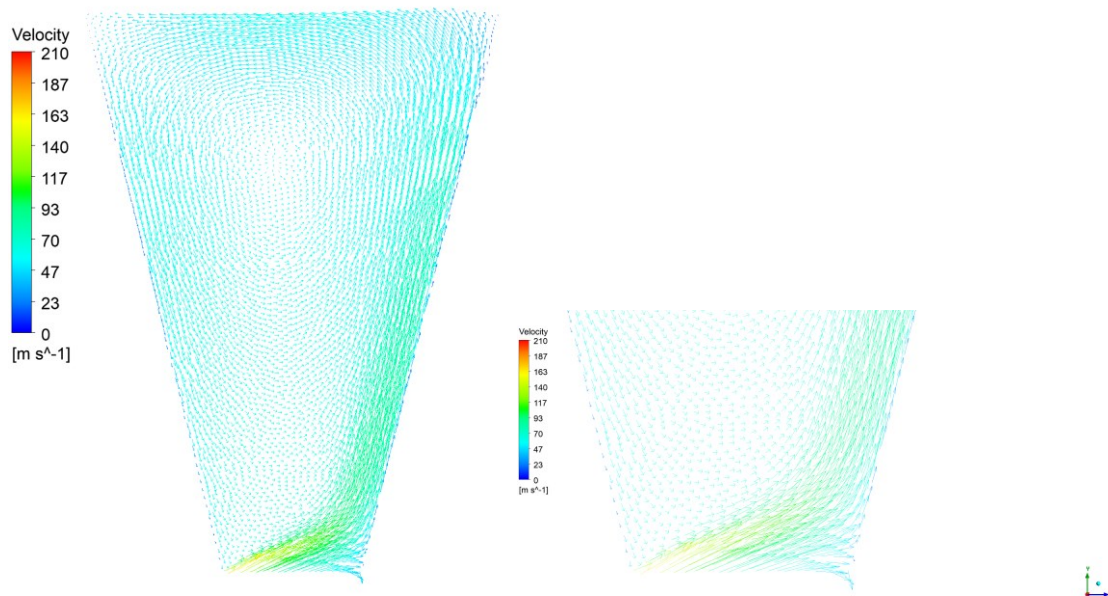


Fig. 26 Velocity contours in bleed domain with 20% of mass flow.

## 5. Conclusions and perspectives

This work marks a significant stride in advancing high-speed, high-temperature turbine technology for innovative energy systems, specifically the negative carbon dioxide gas power plant (nCO<sub>2</sub>PP). By meticulously designing and comparing two distinct turbine configurations, this study illuminates the critical role of bleed pressure and rotational speed in optimizing turbine performance.

The exploration of turbines A and B, differing in a number of stages and rotational speeds but sharing similar inlet and outlet dimensions, reveals nuanced insights into turbine efficiency and power dynamics. Particularly, it demonstrates how turbine A, despite higher base efficiency, encounters a drop in performance at turbine B's nominal speed, underscoring the delicate balance between speed, efficiency, and power output.

The core and at the same time most important findings relate to two facts, namely:

1) The superior controllability of the two-stage turbine is evidenced by the wide range (from 60 000 to 105 000 rpm) of high efficiencies (above 70%, up to an efficiency peak of 81.5%);

2) The two-stage turbine is also less influenced by bleed, which in the case of a five-stage turbine is characterized by a loss of power in the fourth and fifth stages along with the enthalpy not being worked out and thus achieving a higher losses at the turbine exit.

In order to achieve higher efficiency, it is anticipated that the blade channel shape, the number of blades, and the rotational speed will be optimized for several operating points. As evidenced by the above article, such a optimization is essential for achieving high efficiency values across a wide range of operating characteristics for both the turbine and the entire system.

## Acknowledgements

The research leading to these results has received funding from the Norway Grants 2014-2021 via the National Centre for Research and Development.

Article has been prepared within the frame of the project: "Negative CO<sub>2</sub> emission gas power plant" - NOR/POLNORCCS/NEGATIVE-CO<sub>2</sub>-PP/0009/2019-00 which is co-financed by programme "Applied research" under the Norwegian Financial Mechanisms 2014-2021 POLNOR CCS 2019 - Development of CO<sub>2</sub> capture solutions integrated in power and industry processes.

Part of calculations were carried out at the Academic Computer Centre in Gdańsk.





579 **References**

- 580 [1] NASA Goddard Institute for Space Studies, GISTEMP Team, 2023: GISS Surface Temperature  
581 Analysis (GISTEMP), version 4 (2023). data.giss.nasa.gov/gistemp/.
- 582 [2] N.J.L. Lenssen, G.A. Schmidt, J.E. Hansen, M.J. Menne, A. Persin, R. Ruedy, et al.,  
583 Improvements in the GISTEMP Uncertainty Model, *J. Geophys. Res. Atmos.* 124 (2019) 6307–  
584 6326. doi:10.1029/2018JD029522.
- 585 [3] O. Omoyele, M. Hoffmann, M. Koivisto, M. Larra, J.M. Weinand, J. Lin, et al., Increasing the  
586 resolution of solar and wind time series for energy system modeling : A review, 189 (2024).  
587 doi:10.1016/j.rser.2023.113792.
- 588 [4] E. Loth, Wind energy value and deep decarbonization design , what ' s next ?, *Next Energy.* 1  
589 (2023) 100059. doi:10.1016/j.nxener.2023.100059.
- 590 [5] R. Daxini, Y. Wu, Review of methods to account for the solar spectral influence on photovoltaic  
591 device performance, *Energy.* 286 (2024) 129461. doi:10.1016/j.energy.2023.129461.
- 592 [6] U. Tesio, E. Guelpa, V. Verda, G. Manc, A review on multi energy systems modelling and  
593 optimization, 236 (2024). doi:10.1016/j.applthermaleng.2023.121871.
- 594 [7] W.M. Tefera, K.S. Kasiviswanathan, A global-scale hydropower potential assessment and  
595 feasibility evaluations, *Water Resour. Econ.* 38 (2022) 100198.  
596 doi:https://doi.org/10.1016/j.wre.2022.100198.
- 597 [8] C. Forman, I.K. Muritala, R. Pardemann, B. Meyer, Estimating the global waste heat potential,  
598 *Renew. Sustain. Energy Rev.* 57 (2016) 1568–1579. doi:10.1016/j.rser.2015.12.192.
- 599 [9] S. Alshammari, S.T. Kadam, Z. Yu, Assessment of single rotor expander-compressor device in  
600 combined organic Rankine cycle (ORC) and vapor compression refrigeration cycle (VCR),  
601 *Energy.* 282 (2023) 128763. doi:10.1016/j.energy.2023.128763.
- 602 [10] L. Wang, X. Bu, H. Li, Multi-objective optimization and off-design evaluation of organic  
603 rankine cycle (ORC) for low-grade waste heat recovery, *Energy.* 203 (2020) 117809.  
604 doi:10.1016/j.energy.2020.117809.
- 605 [11] D. Mikielewicz, J. Wajs, P. Ziółkowski, J. Mikielewicz, Utilisation of waste heat from the power  
606 plant by use of the ORC aided with bleed steam and extra source of heat, *Energy.* 97 (2016) 11–  
607 19. doi:10.1016/j.energy.2015.12.106.
- 608 [12] T. Ho, S.S. Mao, R. Greif, Comparison of the Organic Flash Cycle (OFC) to other advanced  
609 vapor cycles for intermediate and high temperature waste heat reclamation and solar thermal  
610 energy, *Energy.* 42 (2012) 213–223. doi:10.1016/j.energy.2012.03.067.
- 611 [13] D. Mikielewicz, Method and system for heat regeneration in a thermodynamic cycle with rapid  
612 expansion of steam (Organic Flash Cycle), patent No. PL237871, 2016.
- 613 [14] K. Adamson, T. Gordon, J.K. Carson, Q. Chen, F. Schlosser, L. Kong, et al., High-temperature  
614 and transcritical heat pump cycles and advancements : A review, *Renew. Sustain. Energy Rev.*  
615 167 (2022) 112798. doi:10.1016/j.rser.2022.112798.
- 616 [15] A. Marina, S. Spoelstra, H.A. Zondag, A.K. Wemmers, An estimation of the European industrial  
617 heat pump market potential, *Renew. Sustain. Energy Rev.* 139 (2021) 110545.  
618 doi:10.1016/j.rser.2020.110545.
- 619 [16] P. Carroll, M. Chesser, P. Lyons, Air Source Heat Pumps field studies : A systematic literature  
620 review, *Renew. Sustain. Energy Rev.* 134 (2020) 110275. doi:10.1016/j.rser.2020.110275.
- 621 [17] A.A. Mana, S.I. Kaitouni, T. Kousksou, A. Jamil, Enhancing sustainable energy conversion:  
622 Comparative study of superheated and recuperative ORC systems for waste heat recovery and  
623 geothermal applications, with focus on 4E performance, *Energy.* 284 (2023) 128654.  
624 doi:10.1016/j.energy.2023.128654.

- 625 [18] Negative CO<sub>2</sub> emission gas power plant, (2019). <https://nco2pp.mech.pg.gda.pl/> (accessed May  
626 10, 2024).
- 627 [19] P. Ziółkowski, K. Stasiak, M. Amiri, D. Mikielwicz, Negative carbon dioxide gas power plant  
628 integrated with gasification of sewage sludge, *Energy*. 262 (2023).  
629 doi:10.1016/j.energy.2022.125496.
- 630 [20] M. Uddin, H. Gurgenci, A. Klimenko, Z. Guan, Heat transfer analysis of supercritical CO<sub>2</sub> in a  
631 High-Speed turbine rotor shaft cooling passage, *Therm. Sci. Eng. Prog.* 39 (2023) 101694.  
632 doi:10.1016/j.tsep.2023.101694.
- 633 [21] G. Xu, G. Zhao, Y. Quan, R. Liang, T. Li, B. Dong, et al., Design and optimization of a radial-  
634 axial two-stage coaxial turbine for high-temperature supercritical organic Rankine cycle, *Appl.*  
635 *Therm. Eng.* 227 (2023) 120365. doi:10.1016/j.applthermaleng.2023.120365.
- 636 [22] M. Banaszkiwicz, Numerical investigations of crack initiation in impulse steam turbine rotors  
637 subject to thermo-mechanical fatigue, *Appl. Therm. Eng.* 138 (2018) 761–773.  
638 doi:10.1016/j.applthermaleng.2018.04.099.
- 639 [23] U. Unnikrishnan, V. Yang, A review of cooling technologies for high temperature rotating  
640 components in gas turbine, *Propuls. Power Res.* 11 (2022) 293–310.  
641 doi:10.1016/j.jprr.2022.07.001.
- 642 [24] R.H. Tindell, T.M. Alston, C.A. Sarro, G.C. Stegmann, L. Gray, J. Davids, Computational Fluid  
643 Dynamics Analysis of a Steam Power Plant Low-Pressure Turbine Downward Exhaust Hood, *J.*  
644 *Eng. Gas Turbines Power.* 118 (1996) 214–224. doi:10.1115/1.2816543.
- 645 [25] P. Ziółkowski, S. Głuch, T. Kowalczyk, J. Badur, Revalorisation of the Szewalski's concept of  
646 the law of varying the last-stage blade retraction in a gas-steam turbine, *E3S Web Conf.* 323  
647 (2021) 00034. doi:10.1051/e3sconf/202132300034.
- 648 [26] K. Veerabathraswamy, A. Senthil Kumar, Effective boundary conditions and turbulence  
649 modeling for the analysis of steam turbine exhaust hood, *Appl. Therm. Eng.* 103 (2016) 773–  
650 780. doi:10.1016/j.applthermaleng.2016.04.126.
- 651 [27] Z. Burton, G.L. Ingram, S. Hogg, A Literature Review of Low Pressure Steam Turbine Exhaust  
652 Hood and Diffuser Studies, *J. Eng. Gas Turbines Power.* 135 (2013). doi:10.1115/1.4023611.
- 653 [28] P. Ziółkowski, Ł. Witanowski, P. Klonowicz, S. Głuch, Optimization of the last stage of gas-  
654 steam turbine using a hybrid method, in: *Proc. 14th Eur. Conf. Turbomach. Fluid Dyn.*  
655 *Thermodyn.*, Gdańsk, 2021: pp. 1–12.
- 656 [29] P. Lampart, Ł. Witanowski, P. Klonowicz, Efficiency Optimisation of Blade Shape in Steam  
657 and ORC Turbines, *Mech. Mech. Eng.* 22 (2018) 553–564. doi:10.2478/mme-2018-0044.
- 658 [30] P. Klonowicz, Ł. Witanowski, T. Suchocki, Ł. Jędrzejewski, P. Lampart, Selection of optimum  
659 degree of partial admission in a laboratory organic vapour microturbine, *Energy Convers.*  
660 *Manag.* 202 (2019). doi:10.1016/j.enconman.2019.112189.
- 661 [31] Ł. Witanowski, P. Klonowicz, P. Lampart, T. Suchocki, Ł. Jędrzejewski, D. Zaniewski, et al.,  
662 Optimization of an axial turbine for a small scale ORC waste heat recovery system, *Energy*. 205  
663 (2020) 118059. doi:10.1016/j.energy.2020.118059.
- 664 [32] P. Ziółkowski, J. Badur, H. Pawlak- Kruczek, K. Stasiak, M. Amiri, L. Niedzwiecki, et al.,  
665 Mathematical modelling of gasification process of sewage sludge in reactor of negative CO<sub>2</sub>  
666 emission power plant, *Energy*. 244 (2022) 122601. doi:10.1016/j.energy.2021.122601.
- 667 [33] P. Ziółkowski, P. Madejski, M. Amiri, T. Kuś, K. Stasiak, N. Subramanian, et al.,  
668 Thermodynamic analysis of negative CO<sub>2</sub> emission power plant using aspen plus, aspen Hysys,  
669 and ebsilon software, *Energies*. 14 (2021) 1–27. doi:10.3390/en14196304.
- 670 [34] M. Kaszuba, P. Ziółkowski, D. Mikielwicz, Comparative study of oxygen separation using  
671 cryogenic and membrane techniques for nCO<sub>2</sub>PP, 36th Int. Conf. Effic. Cost, Optim. Simul.

- 672 Environ. Impact Energy Syst. ECOS 2023. (2023) 2903–2914. doi:10.52202/069564-0260.
- 673 [35] K. Stasiak, I.S. Ertesvåg, P. Ziółkowski, D. Mikielewicz, Exergetic Analysis of the nCO<sub>2</sub>PP  
674 Cycle with Particular Reference to the Exergy Destruction of Sewage Sludge Due to  
675 Gasification, in: 36th Int. Conf. Effic. Cost, Optim. Simul. Environ. Impact Energy Syst. (ECOS  
676 2023), ECOS 2023, Las Palmas De Gran Canaria, Spain, 2023: pp. 222–232.  
677 doi:10.52202/069564-0021.
- 678 [36] M. Kaszuba, P. Ziółkowski, D. Mikielewicz, Performance of cryogenic oxygen production unit  
679 with exhaust gas bleed for sewage sludge gasification and different oxygen purities, Arch.  
680 Thermodyn. 44 (2023) 1–19. doi:10.24425/ather.2023.14xxxx.
- 681 [37] K. Stasiak, P. Ziółkowski, D. Mikielewicz, Selected Aspects of Performance of Organic Rankine  
682 Cycles Incorporated Into Bioenergy With Carbon Capture and Storage Using Gasification of  
683 Sewage Sludge, J. Energy Resour. Technol. 146 (2024). doi:10.1115/1.4064196.
- 684 [38] I.S. Ertesvåg, P. Madejski, P. Ziółkowski, D. Mikielewicz, Exergy analysis of a negative CO<sub>2</sub>  
685 emission gas power plant based on water oxy-combustion of syngas from sewage sludge  
686 gasification and CCS, Energy. 278 (2023) 127690. doi:10.1016/j.energy.2023.127690.
- 687 [39] G. Cordes, W. Traupel, Die Theorie der Strömung durch Radialmaschinen. VIII + 160 S. m. 103  
688 Abb. Karlsruhe 1962. Verlag G. Braun. Preis geb. DM 27,—, ZAMM - Zeitschrift Für Angew.  
689 Math. Und Mech. 43 (1963). doi:10.1002/zamm.19630430310.
- 690 [40] P. Klonowicz, F. Heberle, M. Preißinger, D. Brüggemann, Significance of loss correlations in  
691 performance prediction of small scale, highly loaded turbine stages working in Organic Rankine  
692 Cycles, Energy. 72 (2014) 322–330.
- 693 [41] H. Brenner, Navier–Stokes revisited, Phys. A Stat. Mech. Its Appl. 349 (2005) 60–132.  
694 doi:10.1016/j.physa.2004.10.034.
- 695 [42] O. Reynolds, On the Equation of Motion and the Boundary Conditions for Viscous Fluid, Fluid,  
696 Br. Assoc. Sec. A Pap. II. 46 (1883) 132–137.
- 697 [43] J. Badur, M. Feidt, P. Ziółkowski, Neoclassical Navier–Stokes Equations Considering the  
698 Gyftopoulos–Beretta Exposition of Thermodynamics, Energies. 13 (2020) 1656.  
699 doi:10.3390/en13071656.
- 700 [44] P. Radomski et al Computational fluid dynamics simulation of heat transfer from densely packed  
701 gold nanoparticles to isotropic media, Arch. Thermodyn. (2023).  
702 doi:10.24425/ather.2021.138111.
- 703 [45] ANSYS®, Academic Research Mechanical and CFD, Release 23.2, (2023).
- 704 [46] E.W. Lemmon, I.H. Bell, M.L. Huber, M.O. McLinden, NIST Standard Reference Database 23:  
705 Reference Fluid Thermodynamic and Transport Properties-REFPROP, Version 10.0, National  
706 Institute of Standards and Technology, (2018). doi:https://doi.org/10.18434/T4/1502528.
- 707 [47] P. Klonowicz, A. Borsukiewicz-Gozdur, P. Hanausek, W. Kryłłowicz, D. Brüggemann, Design  
708 and performance measurements of an organic vapour turbine, Appl. Therm. Eng. 63 (2014) 297–  
709 303. doi:10.1016/j.applthermaleng.2013.11.018.
- 710 [48] A. Andrearczyk, P. Bagiński, P. Klonowicz, Numerical and experimental investigations of a  
711 turbocharger with a compressor wheel made of additively manufactured plastic, Int. J. Mech.  
712 Sci. 178 (2020). doi:10.1016/j.ijmecsci.2020.105613.
- 713 [49] P. Ziółkowski, Ł. Witanowski, S. Głuch, P. Klonowicz, M. Feidt, A. Koulali, Example of Using  
714 Particle Swarm Optimization Algorithm with Nelder–Mead Method for Flow Improvement in  
715 Axial Last Stage of Gas–Steam Turbine, Energies . 17 (2024). doi:10.3390/en17122816.
- 716 [50] P. Thornley, J. Rogers, Y. Huang, Quantification of employment from biomass power plants,  
717 Renew. Energy. 33 (2008) 1922–1927. doi:10.1016/j.renene.2007.11.011.
- 718 [51] Ł. Witanowski, P. Klonowicz, P. Lampart, P. Ziółkowski, Multi-objective optimization of the

- 719 ORC axial turbine for a waste heat recovery system working in two modes: cogeneration and  
720 condensation, *Energy*. 264 (2023) 126187. doi:10.1016/j.energy.2022.126187.
- 721 [52] H. Li, S. Rane, Z. Yu, Investigation of the performance and flow characteristics of two-phase  
722 reaction turbines in total flow geothermal systems, *Renew. Energy*. 175 (2021) 345–372.  
723 doi:10.1016/j.renene.2021.05.022.
- 724 [53] Y. Chen, Y. Liu, W. Liu, Y. Ge, Y. Xue, L. Zhang, Optimal design of radial inflow turbine for  
725 ocean thermal energy conversion based on the installation angle of nozzle blade, *Renew. Energy*.  
726 184 (2022) 857–870. doi:10.1016/j.renene.2021.12.016.
- 727